nature communications

Article

https://doi.org/10.1038/s41467-024-53302-5

A tissue bandage for pelvic ganglia injury

Received: 21 October 2023

Accepted: 8 October 2024

Published online: 17 October 2024

Check for updates

Jing He[1,2,6], Lin Qian[3,6], Zhuang Li[1], Yanpeng Wang[4], Kai Liu[1], Haibin Wei[3], Yuan Sun[1], Jiaoyan He[5], Ke Yao[1], Jiahao Weng[1], Xuanhan Hu[3], Dahong Zhang[3] ✉ & Yong He[1,2] ✉

Neurogenic bladder often occurs after pelvic ganglia injury. Its symptoms, like severe urinary retention and incontinence, have a significant impact on individuals' quality of life. Unfortunately, there are currently no effective treatments available for this type of injury. Here, we designed a fiber-enhanced tissue bandage for injured pelvic ganglia. Tight junctions formed in tissue bandages create a mini tissue structure that enhances resistance in an in vivo environment and delivers growth factors to support the healing of ganglia. Strength fibers are similar to clinical bandages and guarantee ease of handling. Furthermore, tissue bandages can be stored at low temperatures over 5 months without compromising cell viability, meeting the requirements for clinical products. A tissue bandage was applied to a male rat with a bilateral major pelvic ganglia crush injury. Compared to the severe neurogenic bladder symptoms observed in the injury and scaffold groups, tissue bandages significantly improved bladder function. We found that tissue bandage increases resistance to mechanical injury by boosting the expression of cytoskeletal proteins within the major pelvic ganglia. Overall, tissue bandages show promise as a practical therapeutic approach for ganglia repair, offering hope for developing more effective treatments for this thorny condition.

Neurogenic bladder (NB) is a common sequel of neurological disease, mainly manifesting as early urinary retention and late incontinence[1]. It leads to physical and mental stress, negatively impacting quality of life. NB can be categorized into peripheral types (pelvic plexus damage from pelvic surgery, trauma, radiation therapy, and childbirth) and central types (central nervous system damage from Parkinson's disease, multiple sclerosis, and spinal cord injury)[2,3]. Research on pelvic plexus injury is limited compared to central NB. However, with the increasing detection rates of pelvic diseases, surgical treatment has become more prevalent as the gold standard[2]. Inevitable intraoperative damage to surrounding neural structures can lead to an enhancement of NB occurrences. For example, NB prevalence following prostatectomy ranges from 1% to 87%[4]. 8–80% of patients experience NB after radical hysterectomy[5]. Despite efforts like nerve-sparing surgeries, rectal cancer patients often face voiding issues. Restoring detrusor function and repairing neural control of the pelvic plexus are crucial for NB treatment[6,7]. Current management options for bladder dysfunction include antimuscarinic medications and intermittent bladder drainage[8]. However, effective methods to restore pelvic nerve function are lacking. Bladder bioelectrical stimulation lacks specificity and efficacy[9]. Similarly, sacral nerve stimulation fails to establish the necessary neural connections, making artificial bladder pacing unachievable[10]. There's an urgent need to address the significant impact of persistent NB on patients through neural repair.

A crush injury to the major pelvic ganglia (MPG) in rats serves as a convenient model for studying neurological damage, including NB

[1]State Key Laboratory of Fluid Power and Mechatronic Systems, School of Mechanical Engineering, Zhejiang University, Hangzhou 310027, China. [2]Liangzhu Laboratory, Zhejiang University Medical Center, Hangzhou 311121, China. [3]Urology & Nephrology Center, Department of Urology, Zhejiang Provincial People's Hospital, Affiliated People's Hospital, Hangzhou Medical College, Hangzhou, Zhejiang, China. [4]Center for Reproductive Medicine, Department of Gynecology, Zhejiang Provincial People's Hospital, Affiliated People's Hospital, Hangzhou Medical College, Hangzhou, Zhejiang, China. [5]Department of Postgraduate Education, Jinzhou Medical University, Jinzhou, Liaoning, China. [6]These authors contributed equally: Jing He, Lin Qian.
✉e-mail: zhangdahong88@yeah.net; yongqin@zju.edu.cn

from pelvic surgery or trauma[11]. This model features traumatic ganglionopathy, an acute severe condition affecting the pelvic plexus. Male rats can more easily identify with their larger and more prominent MPG than females. This characteristic reduces the difficulty of surgical modeling and contributes to a more stable model. Additionally, females show more urinary incontinence and minor bladder dilation due to anatomical differences. In contrast, male rats demonstrate severe urinary retention and bladder dilation, making them a more appropriate model for assessing treatment efficacy.

Research indicates angiogenesis can facilitate axon regeneration in nerve injuries by guiding axon sprouting through vascular endothelial growth factor and enhancing neurogenesis in neural stem/progenitor cells[12,13]. Endothelial cells create a conducive microenvironment for intraneural angiogenesis[14]. Promoting the angiogenesis at the injury site holds promise for nerve recovery[15]. Human umbilical vein endothelial cells (HUVECs), a vital endothelial cell line secreting growth factors like VEGFA, have been chosen as therapeutic agents for delivery to MPG[16].

Cell sheet technology is widely used for cell delivery due to its multicellular structures, which help reduce cell loss during delivery and prolong cell survival in vivo[17]. However, their limited mechanical properties restrict their application[18]. The practicality of clinical operations is a crucial factor in product design. Moreover, considering the delicate and intricate nature of the pelvic ganglia, the delivery system must be flexible enough to accommodate tissue structure and prevent additional damage to ganglia. A fiber-enhanced tissue bandage (TB) was developed to address pelvic ganglia injuries.

In this study, we utilized the melt electrowriting (MEW) technique to fabricate a bilayer membrane structure composed of Poly(ε-caprolactone) (PCL)[19]. The design features interwoven mini fibers to enhance fracture resistance and provide suitable pore sizes for cell loading[20]. Additionally, strength fibers were integrated to improve mechanical durability, mimicking clinical bandages for enhanced usability during surgical procedures. Culturing HUVECs on the scaffold resulted in the formation of tight junctions (TJs) resembling mini-tissues, effectively preventing cell leakage and resisting harsh environments. Our application of TB to crushed MPG demonstrated preserved bladder function and reduced urinary retention damage after 2 weeks (Fig. 1). Furthermore, we found that TB could be effectively stored at low temperatures using a serum-free cryopreservation medium (SFCM) for up to 5 months, maintaining its viability and repair effects upon thawing. The elimination of chemical modifications and resource-intensive techniques simplifies the FDA approval process, while PCL's biodegradability adds to its appeal[21]. Overall, this therapeutic approach was deemed straightforward and a promising option for various clinical applications and a convertible product.

Results

TB simulates mini-tissue and can potentially promote angiogenesis

The scaffold comprises a bilayer structure, with the bottom layer designed as a square grid featuring diagonal lines extending in both directions, creating a "✳" shape node between fibers. The top layer consists of strength fibers arranged in a single direction (Fig. 2a). The

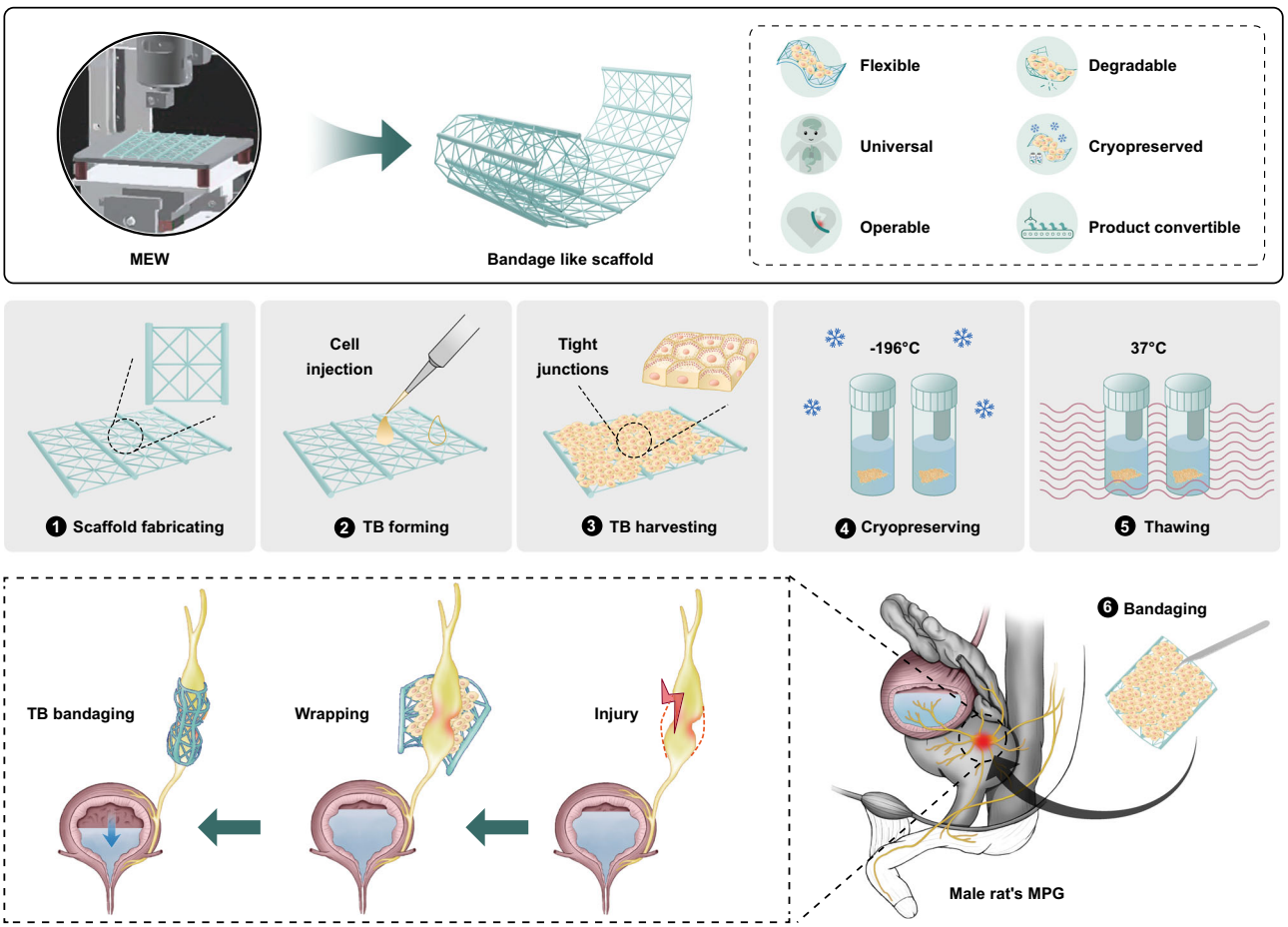

Fig. 1 | Preparation and application of TB. A bandage-like scaffold was successfully fabricated using melt electrowriting (MEW). Seeding cells on the TB yielded a versatile product with attributes such as flexibility, universality, operability, degradability, cryopreservatibility, and convertibility. Then, TB can effectively treat MPG injuries to alleviate NB symptoms in male rat.

https://doi.org/10.1038/s41467-024-53302-5

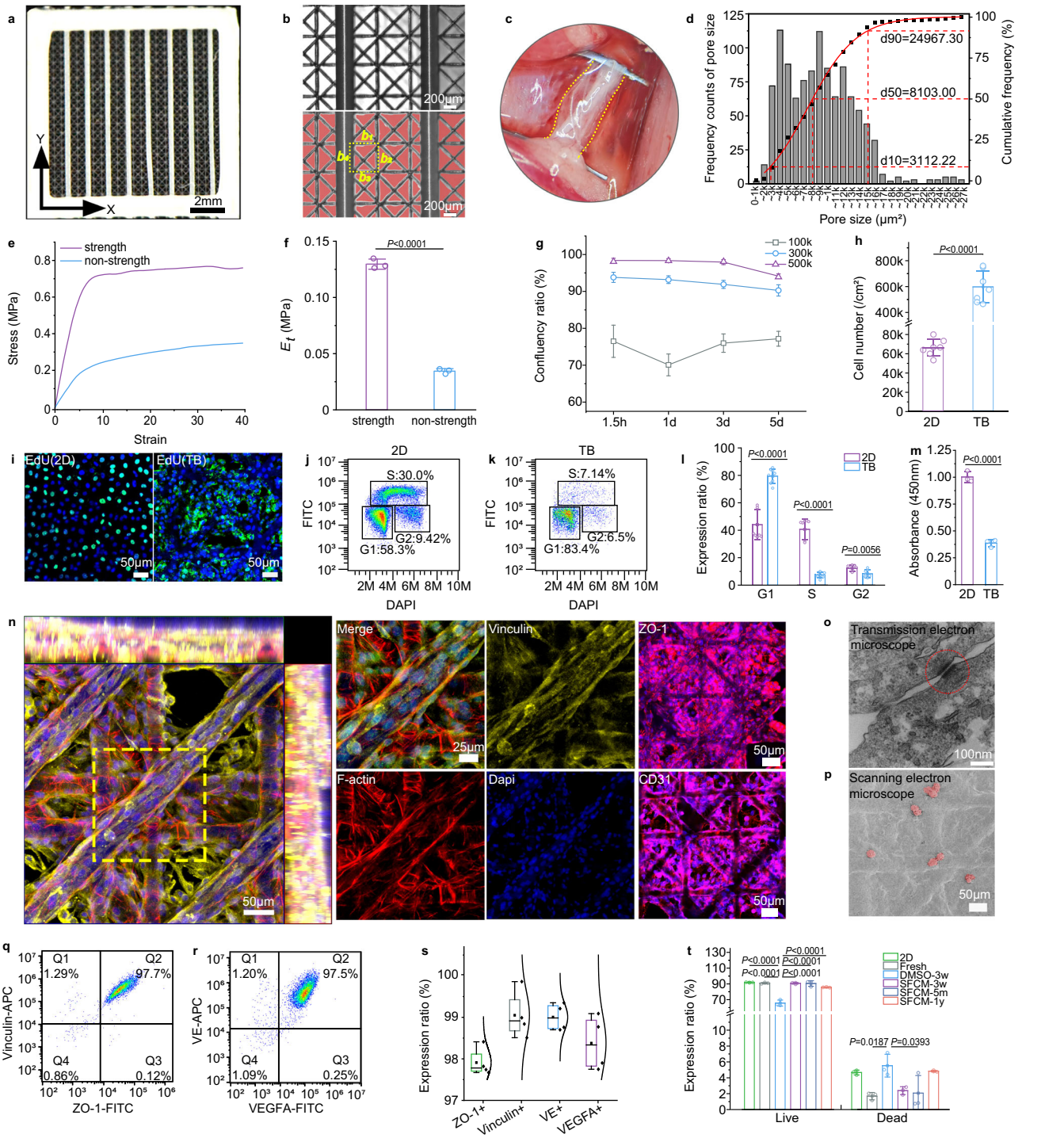

Fig. 2 | Mini-tissue-like properties of TB. a, **b** The scaffold unit morphology and pores are labeled in red (b_1–b_4 represents the single pore in one square). **c** TB wrapped ganglia. **d** Pore size analysis. **e**, **f** Comparison of stress-strain curves and tensile modulus between strength and non-strength scaffold. $n = 3$. **g** Confluency ratio on TB with 100k, 300k, and 500k cell seeding at 1.5 h, 1 day, 3 days, and 5 days. $n = 9$. Data are presented as mean ± SEM. **h** Cell loading capacity between petri dish (2D) and TB. $n = 7$. **i** The EdU images of 2D and TB. **j**, **k** Flow cytometry of cells on 2D or TB with EdU stain. **l** Expression ratio in G1, S, and G2 phase in flow cytometry. $n = 8$. **m** Proliferation evaluation of 2D and TB by CCK8 kit. $n = 3$. **n** TB expressed Vinculin, ZO-1, and CD31. **o** TJs formation on TB, labeled with a red circle. **p** A voidless sheet structure of TB. **q**–**s** Flow cytometry characterization and expression ratio of TB positively defined as VE, VEGFA, ZO-1, and Vinculin. $n = 4$. **t** Live/dead cell comparison among 2D, fresh TB (Fresh), TB thawed from 10% v/v DMSO medium at 3 weeks (DMSO-3w), TB thawed from a serum-free cryopreservation medium (SFCM) at 3 weeks (SFCM-3w), 5 months (SFCM-5m), and 1 year (SFCM-1y). $n = 3$. For bar graphs, data are presented as mean ± SEM. For box plots, box shows median, 25th and 75th percentiles and whiskers represent minima and maxima. A two-tailed *t*-test was employed to compare two groups, followed by multiple comparisons with Bonferroni correction. Comparison involving more than two groups entailed one-way ANOVA, followed by a variance homogeneity test with Levene correction and multiple comparisons with Bonferroni correction. Source data are provided in NC._data_file_s1.

basal mini fibers have an average diameter of 27.90 ± 2.49 μm, with the 45° gap measuring 186.66 ± 8.60 μm and the 90° gap measuring 279.06 ± 11.08 μm. The strength fibers have 167.99 ± 7.39 μm diameter and a gap of 814.45 ± 41.89 μm (Fig. 2b). It provides the ability for the bandage to roll on one axis, similar to bandages used in clinical settings that can easily wrap around the ganglia (Fig. 2c). However, the pore size is uneven within one square, due to the limitation of printing accuracy and the addition of strength fibers (Fig. 2b). The frequency of pore size has distinct peaks at 2-3k and 7-8k (Fig. 2d). The cumulative frequency of pore size could be effectively fitted by the Sigmoidal-Boltzmann model (adjusted R^2 exceeding 99.77%), leading to the derivation of formula (1):

$$y = A2 + \frac{A1 - A2}{1 + e^{(x-x0)/dx}} \quad (1)$$

where $A1$ is the initial value, $A2$ is the final value, $x0$ is the center, and dx is the time constant. Specifically, $A1 = -12.78$, $A2 = 100.41$, $x0 = 7.42$, $dx = 3.12$.

The cumulative frequencies of 10% (d10), 50% (d50), and 90% (d90) illustrate that the primary size distribution falls in the range of 3.11k–24.97k.

The scaffold provides excellent resistance to stretching, strength fibers exhibiting a tensile modulus 3.77 times higher than non-strength fibers due to their larger diameter. These added strength fibers also limit rolling in one direction, similar to clinical bandages, enhancing user-friendliness (Fig. 2e, f and Supplementary Movie 1). Supplementary Movie 2 showcases the TB fabrication process, which is simple and replicable, akin to standard cell culture practices (Fig. S1a–d). After analyzing different cell seeding densities, we found that using 300k cells minimized cell loss compared to 100k and 500k (Fig. S2b, c). This approach maintained over 90% cell fusion and reached 500k cells per unit within 5 days (Figs. 2g and S2a, d). In contrast, there is a decrease in both fusion efficiency and cell count over time in the 500k cell group. Therefore, 300k cells was employed for TB construction by the evidence of cell loss and fusion rates. The mature TB can accommodate over 5.97×10^5 cells/cm^2, approximately 9.01 times more than petri dish (2D) can hold (Fig. 2h). Subsequent evaluation using an EdU kit showed that cells within TB maintained a high proportion in the G1 phase and a low proportion in the S and G2 phase (Fig. 2i–l). Furthermore, CCK8 analysis confirmed low proliferation rates in TB (Fig. 2m). These findings underscore the presence of contact inhibition in TB, a crucial factor for cell integration and assessing TB's safety to prevent tumor formation in vivo[22].

After 5 days of cultivation, the cells were firmly attached and well-integrated with each other. To verify its maturity, we evaluated the expression of vascular endothelial-related proteins in the TB. As depicted in Fig. 2n, cells were evenly spread on the bandage and showed endothelial markers like CD31, ZO-1, and Vinculin, indicating a mature and functional HUVECs phenotype on the scaffold[23–25]. CD31 is crucial for identifying endothelial cells and maintaining cell-cell junction integrity on TB[24]. Vinculin plays a pivotal role in cell-cell connections and ECM stability[2]. ZO-1 is a marker for barrier function in forming TJs[26]. Endothelial solid cell-cell junctions, cytoskeletal organization, and barrier function are essential for endothelial cell function in mimicking vascular tissue and enhancing TB survival in challenging in vivo environments[23]. Additionally, transmission electron microscope confirmed the presence of TJs in TB (Fig. 2o)[27]. These results provide initial evidence of successful mini-tissue construction.

The bottom layer provides both mechanical strength and anchors for cell adhesion, growth, and migration, forming a holistic cell bandage (Fig. 2p). A micro 3D structure within a scaffold effectively houses many cells arranged in layers (Fig. S3a). Vesicular structures on TB measuring approximately 346.17 ± 37.78 nm in diameter, aligning with the characteristic size of exosomes (Fig. S3b)[28]. Cell migration with pseudopodia on the bandage is similar to vehicles navigating a highway (Supplementary Movie 2 and Fig. S3c). Additionally, flow cytometry reveals intercellular connections and angiogenesis-promoting functions in TB, with ZO-1, Vinculin, VE (an endothelial barrier protein controlling endothelial permeability and leukocyte transmigration), and VEGFA all exceeding 97% (Fig. 2q–s)[29]. These findings bolster the concept that TB exhibits characteristics akin to mini-tissue.

Cryopreservation is a crucial process for TB applications. We found that a commercial SFCM is superior to the conventional 10% v/v DMSO method, resulting in significantly lower cell shedding and a reduced ratio of dead cells, preserving TB viability for up to 5 months (Figs. 2t and S4a, b). This method meets the clinical storage needs for TB products. After TB implantation, PCL triggers a foreign body reaction, recruiting macrophages for digestion and absorption. Initially, PCL degrades via ester bond hydrolysis into fragments encapsulated in 1k–6k nm^2 vesicles (Fig. S5a, b). Evaluation of fiber area shows a decrease at the early stage, followed by an increase after 6 weeks as neighboring fibers fuse with the integration of foreign-body giant cells (Fig. S5c, d). PCL degrades into ε-caprolactone and hydroxyhexanoic acid, which are metabolized into CO_2 and water without significant toxicity, confirming PCL's safety for in vivo use[21]. These features make TB suitable for clinical use as a cell delivery product.

RNA-sequencing (RNA-seq) analysis demonstrated a distinctive variation in gene expression patterns between cells on TB and 2D (Fig. 3a). A total of 999 significant differentially expressed genes were obtained, including 548 up-regulated genes and 451 down-regulated genes (Fig. 3b). The Gene Ontology (GO) analysis suggested that these genes mainly enriched in angiogenesis, hypoxia, and ECM remodeling (Fig. 3c). The Kyoto Encyclopedia of Genes and Genomes (KEGG) enrichment results showed that the HIF-1 signaling pathway was promoted, which indicates a hypoxia status in TB (Fig. 3d). Since a high cell density within TB induces a hypoxic microenvironment that triggers elevated expression of VEGFA. VEGFA upregulation enhances the angiogenic capabilities of HUVECs to improve oxygen acquisition[30]. Then, we extracted genes related to angiogenesis function. The comparison showed that these genes are mostly positively correlated (Fig. 3e). We found TB exhibited a substantial increase in VEGFA expression, exceeding that of the 2D culture by more than 4-fold. Moreover, the upregulation of proliferation and development genes (FOS, JUNB, and WNT5A) alongside neurotrophic and neuroprotective genes (F3, ENO2, and DNER) in TB further supports its potential for neuronal repair (Fig. 3f)[31–35]. Accordingly, it seems that TB could be a potential strategy for therapy of impaired MPG.

TB regulates voiding behavior and bladder function after MPG injury

The essential surgical procedure involved exposure, separation, crushing, insertion, and bandaging. Post-crushing, a noticeable impression was observed on MPG (Fig. 4a). Therapeutic efficacy was evaluated after 2 weeks. The injury and scaffold groups showed signs of urinary retention, such as significant bladder enlargement and increased residual urine. Additionally, the injury group showed diverticula. In contrast, the TB group displayed moderate bladder size and residual urine levels (Fig. 4b, c).

Behaviorally, void spots in the sham group were concentrated in two corners with larger spot areas, indicating effective bladder voiding and emptying capacity. The void spots in the scaffold and injury groups were randomly distributed, with smaller spot sizes and higher counts, indicating filling incontinence and loss of voluntary voiding (Fig. 4d–f). Similar to the sham group, the TB group had void spots mainly in corners but smaller and scattered, suggesting partial recovery of impaired voiding function. There was no significant difference in total spot area (Fig. 4e).

Urodynamic tests revealed distinct urinary patterns among the different groups. The sham group exhibited standard urination

https://doi.org/10.1038/s41467-024-53302-5

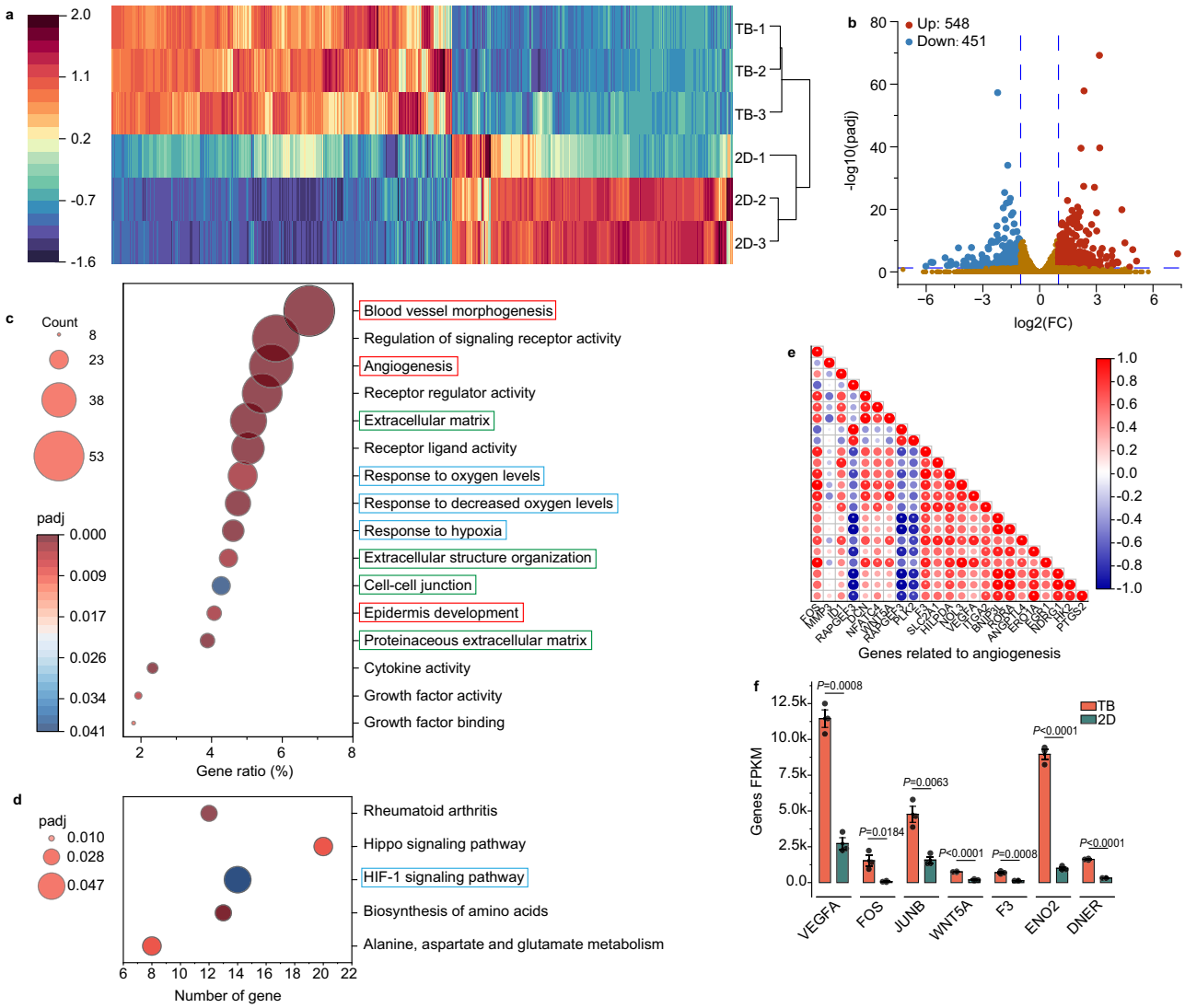

Fig. 3 | RNA-seq analysis between TB and 2D culture. a A heatmap of the differential gene expression. Red indicates high expression, and blue indicates low expression. **b** Volcano plot to identify genes that had a log2(fold-change, FC) value > 1 or <−1 and $p < 0.05$. **c** GO enrichment plot of the differential significantly expressed genes. The red box is related to angiogenesis terms, the blue box is related to hypoxia terms, and the green box is related to ECM remodeling terms. **d** KEGG enrichment plot of the pathway. The blue box is related to the hypoxia pathway. **e** Correlation heatmap of differential genes with angiogenesis. **f** Analysis of noteworthy genes. Fragments Per Kilobase per Million (FPKM). $n = 3$. To identify genes with significant changes in expression levels, we start by standardizing readcount. Next, we calculate the p value using the negative binomial distribution for hypothesis testing. Finally, we use Bonferroni correction to obtain the adjusted p value ($p$adj). For bar graphs, data are presented as mean ± SEM. A two-tailed t-test was employed to compare two groups, followed by multiple comparisons with Bonferroni correction. Source data are provided in NC._data_file_s1.

patterns characterized by effective contraction peaks (ECP) during urination and a well-regulated urine output cycle. In contrast, the TB group demonstrated prolonged voiding intervals and reduced frequency despite showing ECP, signifying delayed nerve conduction. Meanwhile, the scaffold and injury groups showed reduced urine volumes, with stable bladder pressure during perfusion and no noticeable ECP (Fig. 4g). However, instances of irregular urine overflows hinted at urine retention and incontinence, early signs of NB after MPG injury. There were no significant variances in baseline pressure across all groups. The scaffold and injury groups exhibited decreased ECP compared to the sham and TB groups (Fig. 4h). The ECP variation is significantly different. The total voiding times in these groups was higher than TB group, primarily due to urinary leakage (Fig. 4i). The TB group, experiencing delayed nerve signal conduction, displayed increased effectual urine output (EUO) compared to other groups, including max, mean, and total EUO (Fig. 4j). The cryopreservation TB also showed effective repairment (Fig. S6a–c). In summary, the TB group maintained the ability of voluntary voiding, while the scaffold and injury groups lost it.

TB mitigates histomorphology changes in the bladder

Bladder morphology analysis revealed significant inflation following MPG injury in all groups except the sham group. The inflation observed in the TB group was relatively minor. Continuous fullness following MPG injury led to increased bladder compliance, accompanied by thinning and remodeling of the bladder wall, and shallow mucosal folds (Fig. 5a). The scaffold and injury groups exhibited prominently damaged and denuded urothelium, compromising barrier function and potentially triggering bladder inflammation (Fig. 5b, c)[36,37]. A notable reduction in mucosal thickness and transitional columnar epithelium of pan Cytokeratin (CKpan) expression was observed (Fig. 5d, e). In contrast, the TB group maintained higher mucosal thickness and an intact epithelial layer. The increased bladder pressure from urinary retention causes damage and atrophy of the bladder

https://doi.org/10.1038/s41467-024-53302-5

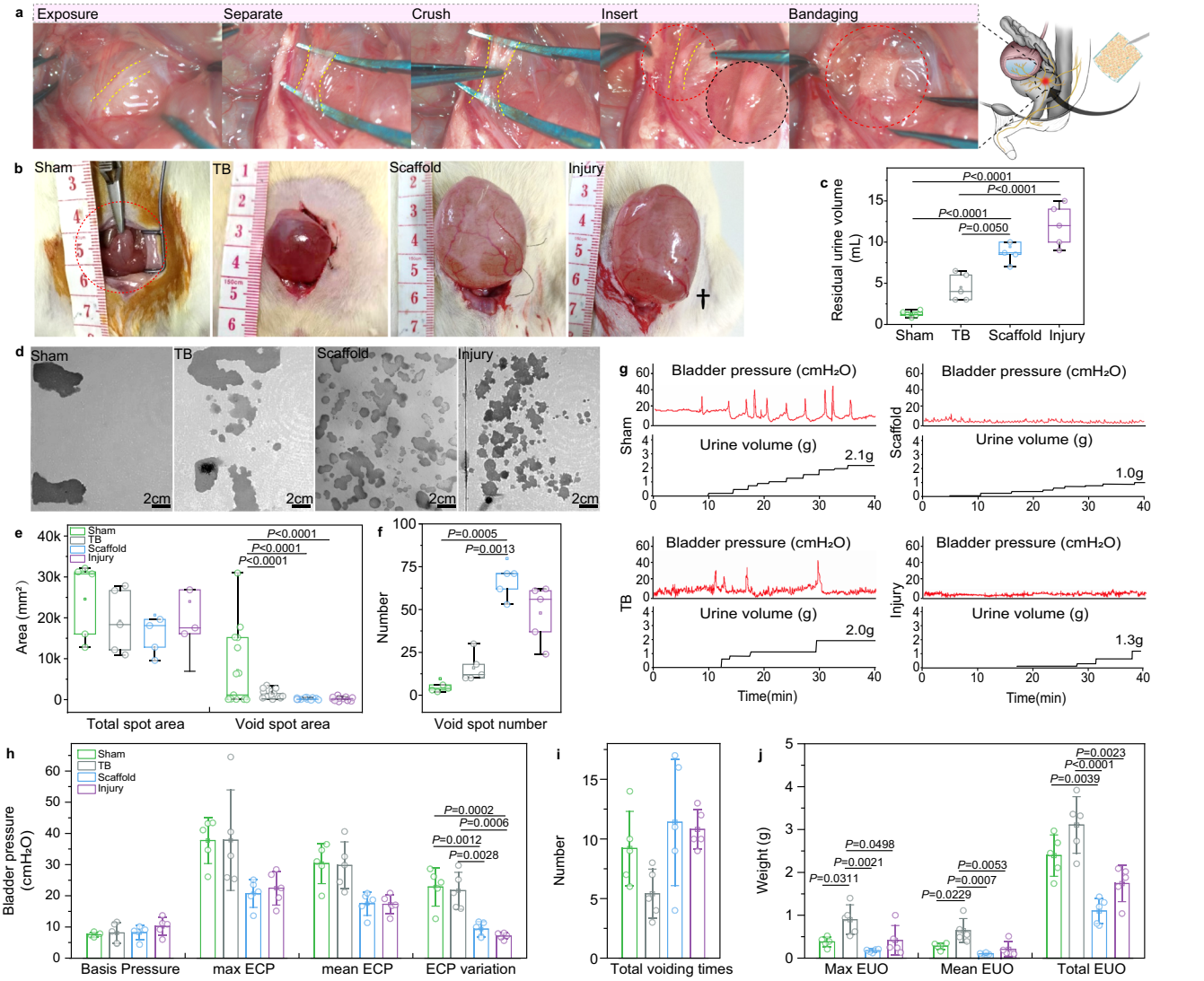

Fig. 4 | The voiding behavior and urodynamic analysis 2 weeks later. a The surgical procedure includes the steps of exposure, separation, crushing, insertion, and bandaging. The impression site was highlighted with black circle. **b** Morphology change of bladder. Diverticulum was labeled by †. **c** Residual urine volume 2 weeks later. $n = 5$. **d** The void spot distribution of all groups. **e**, **f** Analysis of void spot assay, including the total spot area, void spot area, and void spot number. $n = 5$. The number of void spot area varies as the behavior changes. **g** Urodynamic testing 2 weeks post-surgery. **h**–**j** Urodynamic analysis included baseline pressure, max effective contraction peak (max ECP), mean ECP, ECP variation, total voiding number, max effectual urine output (max EUO), mean EUO, and total EUO. $n = 5$. For bar graphs, data are presented as mean ± SEM. For box plots, box shows median, 25th and 75th percentiles and whiskers represent minima and maxima. One-way ANOVA followed by a variance homogeneity test with Levene correction and multiple comparisons with Bonferroni correction. Outliers exceeding upper and lower limits are removed based on box plot analysis. Source data are provided in NC._data_file_s1.

muscle, resulting in decreased muscle content within the bladder muscle layer. This effect intensifies at 4 weeks, manifested as widening of muscle space and fibrous tissue deposition. However, collagen deposition slightly increases in the bladder of scaffold and injury groups at 4 weeks, suggesting a longer time may be needed for full fibrosis development (Fig. S7a–d). As expected, vessel distribution also varied, with the TB group showing increase in expression compared to the sham and injury groups (Fig. 5f, g). The cryopreserved TB demonstrated the ability to protect bladder structure (Fig. S6d, e). In conclusion, MPG injury had a detrimental impact on bladder structure, but TB therapy mitigated these effects, suggesting its potential in preserving it.

TB protects the MPG and supports its recovery

MPG serves as a vital neural structure, acting as a relay station for signal transmission[38,39]. Its health is crucial for downstream organ function. Luciferase imaging revealed that TB can survive for approximately 5 days in vivo, indicating its involvement in early repairment stage (Fig. S8a, b). In Fig. 6a, b, the sham group exhibited well-organized MPG morphology with neatly distributed neural bodies and randomly scattered small vessels. In contrast, the TB, scaffold, and injury groups showed disruptions in morphology, decreased neuron numbers, inflammatory infiltration, and hemorrhage. Even in the injury group, necrosis and fibrosis were observed, while the scaffold group displayed neutrophil infiltration. Nissl bodies play a crucial role in protein synthesis within neurons. Toluidine blue staining revealed neuronal damage in all groups, except for the sham group. The scaffold and injury groups exhibited more severe conditions, including degradation, deformation, vacuolization, and decreased cellular contents (Figs. 6c and S9a). This is further supported by Fig. 6f, which shows reduction in Nissl bodies in the scaffold and injury groups compared to the sham and TB groups. In Fig. 6d, compared to the typical arterial and venous concomitant flow in sham group, the other groups exhibited smaller vessels and higher vessel density. Additionally, the

https://doi.org/10.1038/s41467-024-53302-5

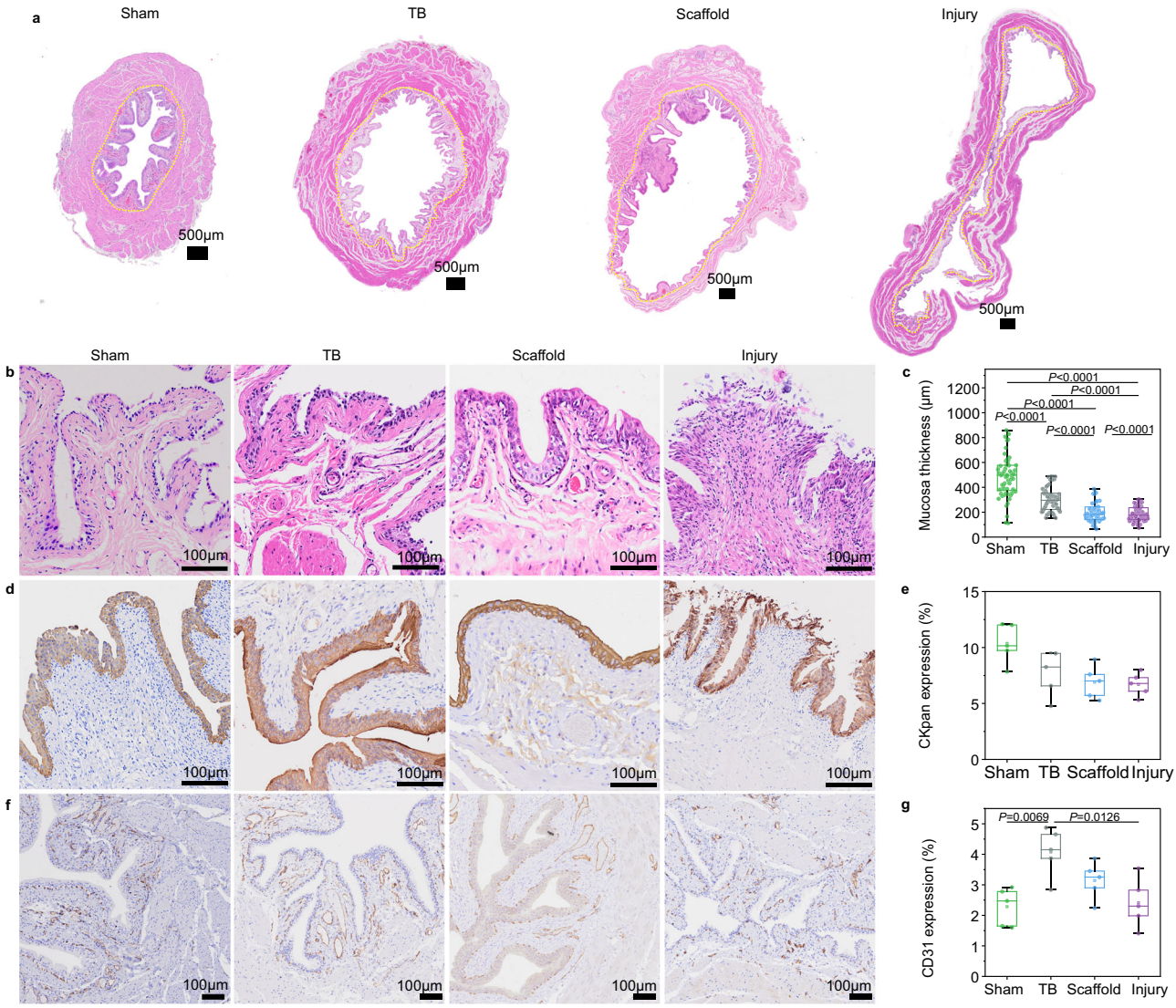

Fig. 5 | Histomorphology change of bladder 2 weeks later. a Overview of H&E staining of bladder morphology. Yellow dots marked the boundary of bladder mucosal layer and muscular layer. **b**, **c** Representative view of bladder mucosal layer and analysis of its thickness per slice. $n = 61$ in 5 rats. **d**, **e** IHC staining of pan Cytokeratin (CKpan) and analysis of its expression in mucosal layer per field. $n = 5$. **f**, **g** Representative view of IHC staining of CD31 and its expression analysis in the bladder per field. $n = 5$. For box plots, box shows median, 25th and 75th percentiles and whiskers represent minima and maxima. One-way ANOVA followed by a variance homogeneity test with Levene correction and multiple comparisons with Bonferroni correction. Outliers exceeding upper and lower limits are removed based on box plot analysis. Source data are provided in NC._data_file_s1.

TB group displayed constriction in small arteries. Further analysis of CD31 expression revealed upregulation of blood vessels in the TB group, validating the RNA-seq results indicating TB's promotion of local neovascularization (Figs. 6g and S9b, c). The thawed TB can also protect MPG (Fig. S6f, g).

The severity of peripheral nerve injuries hinges on demyelination and the extent of axonal and connective tissue damage[40]. In Fig. 6e, the sham group showed normal myelinated axons, mitochondria (mit), and compact myelin sheath (MS). The injury and scaffold groups showed severe axonal degeneration, containing loss of axons, an irregular laminated structure of MS, reduced volume, myelin debris, and absence of mit. While the TB group maintained a certain number of axons, there were irregularities in the MS and decreased volume and mit number. We speculate that TB facilitates microvasculature involvement with myelinating glial cells regeneration, protects axon and MS through neurotrophic assistance[41].

The G-ratio is a critical measure associated with nerve impulse conduction velocity, showing a positive correlation[42]. In the sham group, the average G-ratio was 0.74 ± 0.02. The injury and scaffold groups had lower G-ratios of 0.42 ± 0.02 and 0.51 ± 0.03, leading to a disorder of signal conduction. However, TB treatment maintained the G-ratio at 0.72 ± 0.02, mitigating the negative effects (Fig. 6h). Analysis of the G-ratio perimeter and area indicated that the injury and scaffold groups displayed abnormal thickening of the MS compared to the sham and TB groups, due to the relaxation of the sheath structure caused by axonal degeneration and clearance of myelin debris (Fig. 6i).

MPG is a complex ganglia that innervates the pelvic organs in rats. It consists of sympathetic and parasympathetic neurons, sensory neurons, interneurons, and possibly enteric neurons, all working in concert to regulate pelvic organ functions[43]. Tuj1 is a specific marker to identify neuron presence and distribution. Our observations revealed a patchy pattern of Tuj1-marked neurons within the MPG. This pattern was consistent across the sham, TB, and scaffold groups, while the injury group significantly reduced expression levels (Fig. 7a).

https://doi.org/10.1038/s41467-024-53302-5

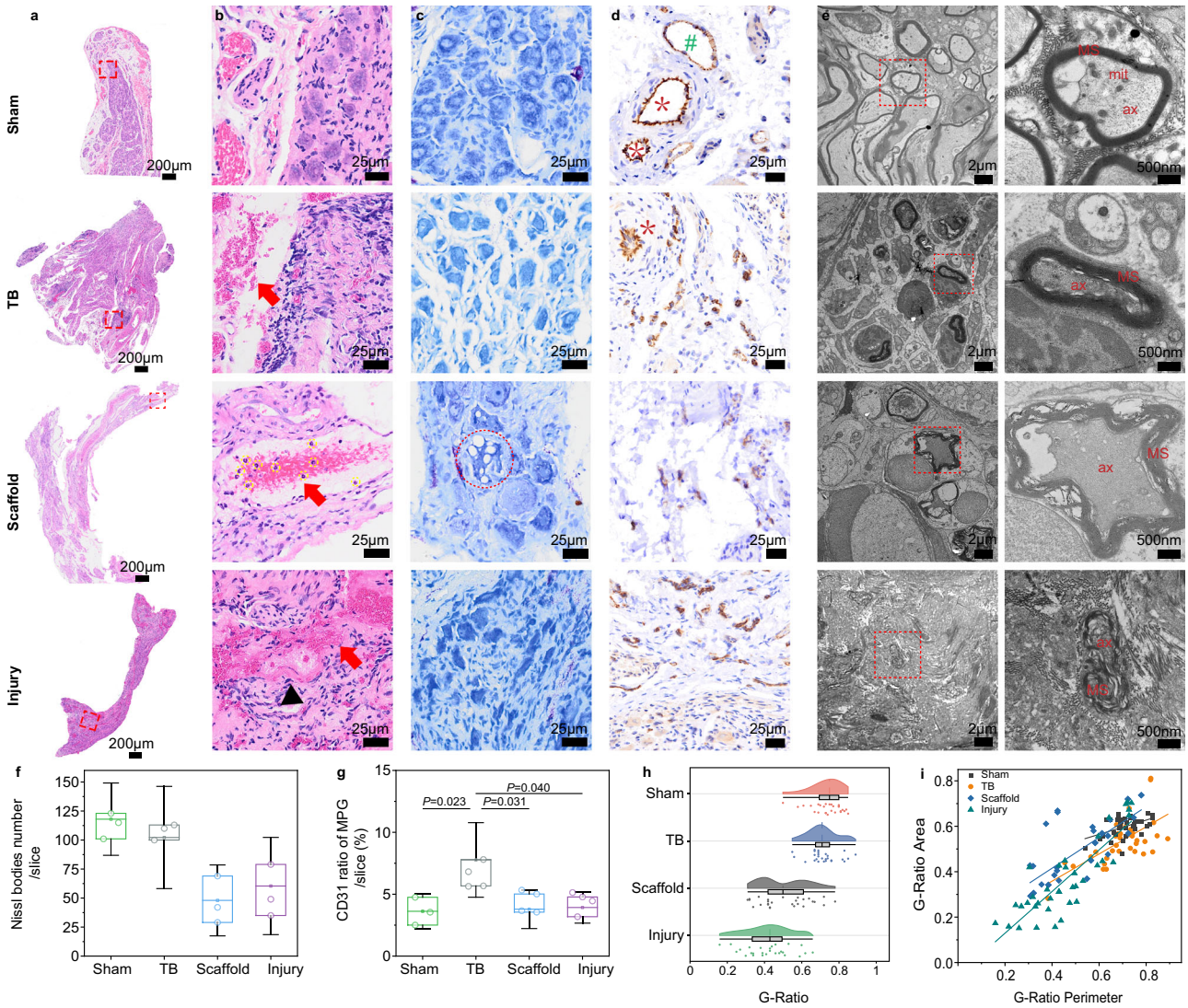

Fig. 6 | Histomorphology changes and axon variations in MPG at 2 weeks. **a**, **b** The overview morphology and representative H&E images of MPG. Bleeding is labeled by →, necrosis is indicated by ▲, and neutrophil infiltration is labeled by the yellow dot. **c**, **f** Nissl bodies stained by toluidine blue in MPG and analysis of its quantity per slice. $n = 5$. Vacuolization is indicated by the red dot. **d**, **g** IHC images of CD31 and expression in MPG per slice. Arteriole labeled by * and venule labeled by #. $n = 5$. **e** TEM micrograph of myelinated axons (ax), mitochondria (mit), and myelin sheath (MS) in MPG. **h** G-Ratio raincloud plot with a box, box shows median, 25th and 75th percentiles and whiskers represent minima and maxima. $n = 27$ in 4 MPGs. **i** Correlation between G-Ratio perimeter and G-Ratio area. $n = 27$ in 4 MPGs. For bar graphs, data are presented as mean ± SEM. For box plots, box shows median, 25th and 75th percentiles and whiskers represent minima and maxima. One-way ANOVA followed by a variance homogeneity test with Levene correction and multiple comparisons with Bonferroni correction. Outliers exceeding upper and lower limits are removed based on box plot analysis. Source data are provided in NC._data_file_s1.

Calcitonin Gene-Related Peptide (CGRP) is a marker for specific sensory neurons[44]. Tyrosine Hydroxylase (TH) is an enzyme critical for catecholamine synthesis to identify sympathetic neurons[45]. S100β is widely recognized as a marker for Schwann cells, reflecting neuron survival and health status[46]. Choline Acetyltransferase (ChAT) is essential for acetylcholine synthesis and specifically marks cholinergic neurons, including those of the parasympathetic system[47]. Enteric cholinergic neurons also express ChAT[48]. Nestin is an intermediate filament found in neuroepithelial stem cells[49]. NF200 is used to identify mature neurons. Neuronal nitric oxide synthase (nNOS) is a crucial enzyme for nitric oxide production and a specific marker for interneurons[50]. Additionally, c-Fos is employed as an indicator of neuronal activity[51]. These markers have been instrumental in identifying and visualizing various neuronal populations within the MPG.

Figure 7b–d depicts intertwined neurofilaments collectively enveloping the body of neuron within the MPG. Tuj1, S100 β, and NF200 markers exhibited higher expression levels across all groups than other markers. Activation of neural stem cells was observed in all groups, as evidenced by the expression of Nestin. The functional neuron markers, including CGRP, TH, ChAT, and nNOS, were positively expressed in both the sham and TB groups; however, their expression levels were reduced in the TB group. In contrast, the expression levels of functional neurons and neurofilaments in the injury and scaffold groups were significantly diminished or absent, indicating severe damage to the MPG. The MPG in the TB group maintained a favorable condition, with functional neurons present at appropriate levels, thereby ensuring proper functionality.

The potential mechanism of MPG injuring and repairing

Cell therapies have great potential for treating diseases, but the need to understand their biological mechanisms hampers product approval and slows progress in the field[52]. Proteomics is a crucial strategy for

https://doi.org/10.1038/s41467-024-53302-5

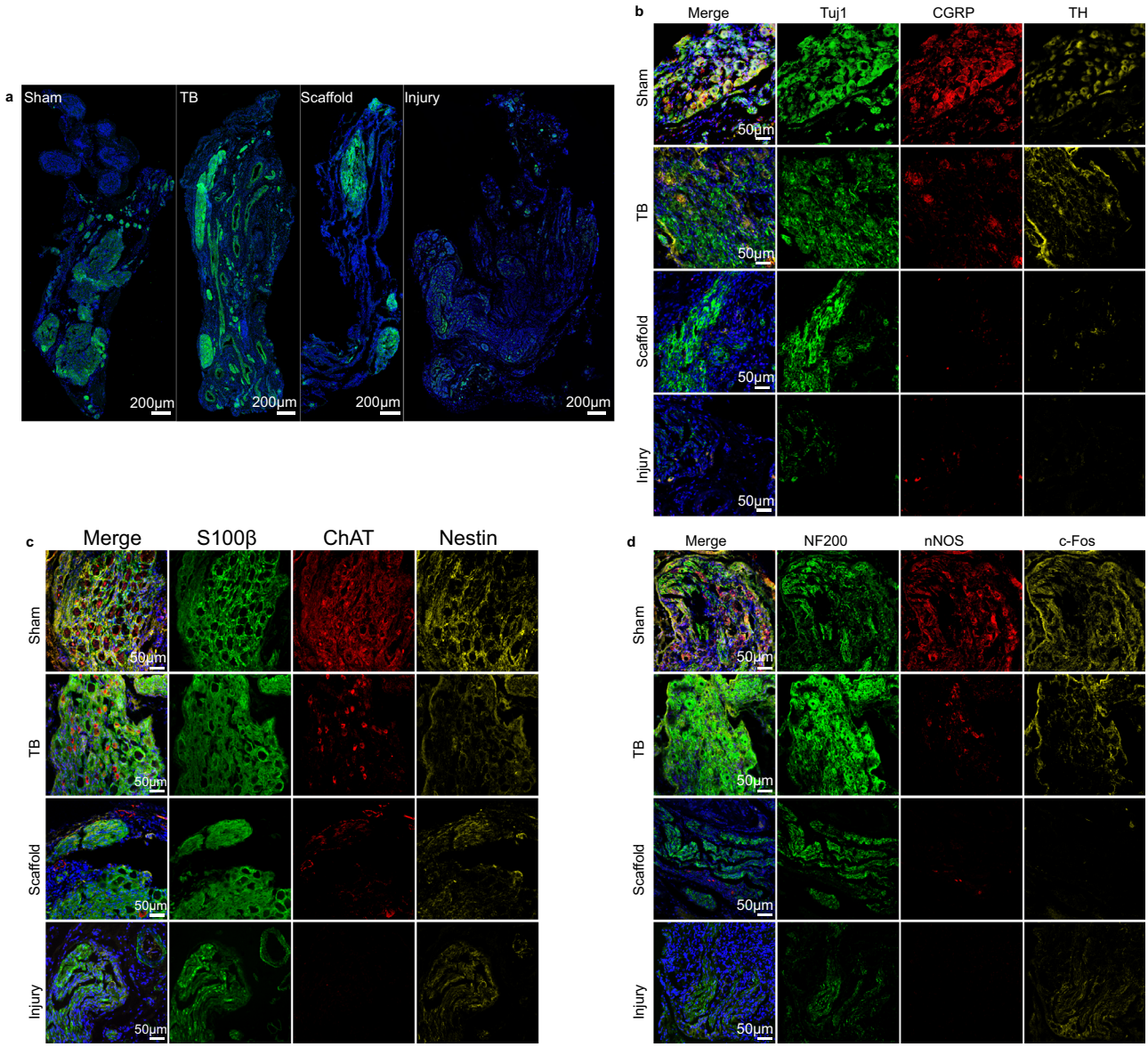

Fig. 7 | Intertwined neural structures in MPG. a Overview images of neurons distribution labeled by Tuj1 in MPG. **b**–**d** Confocal images revealed the presence of functional neurons (Tuj1, CGRP, TH, S100β, ChAT, Nestin, NF200, nNOS, and c-Fos) in MPG.

learning disease progression. Based on our results, the scaffold acts as a delivery tool for HUVECs transplantation without repairing MPG. Therefore, we conducted Tandem Mass Tags (TMT) Proteomics analysis on sham, TB, and injury groups. The data showed good repeatability and stability (Fig. S10a–d). A total of 329 significant differential expression proteins (DEPs) were identified. From the subcellular localization, they are clustered with 24.96% nucleus protein, 22.99% cytoplasm protein, and so on (Fig. S10e).

By comparing the sham group and the injury group, a total of 144 DEPs were found, including 83 up-regulated and 61 down-regulated (Figs. 8a and S10f). GO enrichment indicated that 74 of 144 DEPs were enriched in 27 GO terms (Fig. 8b). We have identified several possible causes of damage, including ion transport disorder, immune response, cellular structural damage, lipid metabolism disorders, ischemia, and oxidative stress. KEGG analysis mainly focused on immune response (Fig. 8c). The Protein-Protein Interaction (PPI) network of DEPs was constructed using the STRING database. Its protein topology further categorized the causes of damage into four categories: neural cell structural and functional disorder (most proteins downregulated), immune response (most proteins upregulated), fatty acid metabolism disorder (downregulated proteins), and others (Fig. 8d). We provided related heatmaps for each PPI network to visualize the related protein interactions (Fig. 8e). Overall, crush to MPG is mechanical damage that triggers many adverse effects, including severe cytoskeletal changes, a robust immune response, homeostasis disruptions, a lipid metabolism disorder, and oxidative stress.

Comparing the MPG from the TB group to the injury group, we identified 79 DEPs, with 58 up-regulated and 21 down-regulated (Figs. 9a and S10g). GO analysis revealed that the DEPs were mainly associated with the cytoskeleton, structural molecule activity, and cell redox homeostasis (Fig. 9b). KEGG pathway analysis focused on muscle contraction (Fig. 9c). PPI network and related heatmap were categorized into cytoskeleton reorganization, keratins, and other classifications (Fig. 9d, e). To assess the immune status in the TB group, we implanted TB in MPG and compared it with sham group. As shown in Fig. S11a, there was an increase in macrophage markers (CD86 for pro-inflammatory and CD206 for anti-inflammatory), indicating initiation of the immune response[53]. While, the significantly higher expression of CD206 suggested an anti-inflammatory reaction in the MPG of the TB group (Fig. S11b, c). These findings suggest that TB has a

https://doi.org/10.1038/s41467-024-53302-5

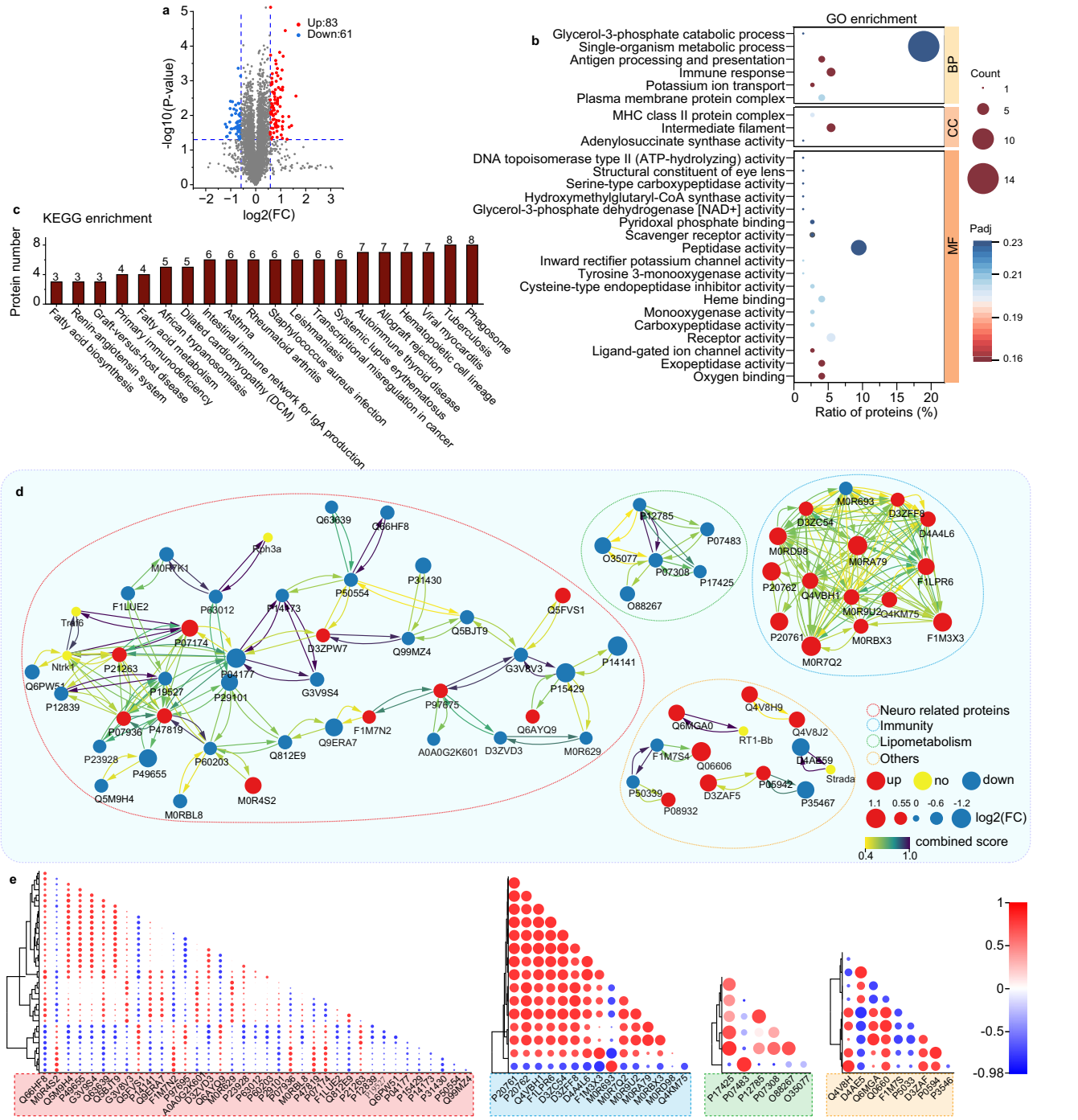

Fig. 8 | TMT analysis uncovers the causes of crush injury to MPG between the injury and sham groups. a Volcano plots of differential expression proteins (DEPs) between two groups. **b**–**d** GO, KEGG enrichment, and PPI network of DEPs between two groups. Neuro related proteins circled by red dot line, immunity circled by blue dot line, lipometabolism circled by green dot line, and others by yellow dot line. **e** The related heatmaps are based on the Protein-PPI topology network. Red dots indicate up-regulated proteins, yellow dots indicate no significant change proteins, and blue dots indicate down-regulated proteins. The dotted line color corresponds with the PPI categories. $n = 3$. A two-tailed t-test was conducted on the relative quantitative values of each protein in two comparison samples, followed by multiple comparisons with Bonferroni correction. Upregulated proteins: FC ≥ 1.5 and p value ≤ 0.05. Downregulated proteins: FC ≤ 0.67 and p value ≤ 0.05. Source data are provided in NC._data_file_s1.

propensity to trigger protective responses in MPG. By responsing to mechanical stimulation, TB enhances the synthesis of cytoskeletal proteins to improve structural stability and mechanical support for cells, aiding in preserving cellular homeostasis, mitigating the impact of external forces, and preventing further damage. Additionally, keratins, which are the primary intermediate filament proteins, enhance cellular mechanical strength and support neuron regeneration and recovery[54]. These findings underscore the effectiveness of TB therapy in promoting cytoskeletal reorganization for MPG repair.

Discussion

We have developed a mini-tissue-like bandage that leverages cell therapy and a 3D-printed scaffold to repair pelvic ganglia injuries. The scaffold structure of the mini-fiber features suitable pore sizes for

https://doi.org/10.1038/s41467-024-53302-5

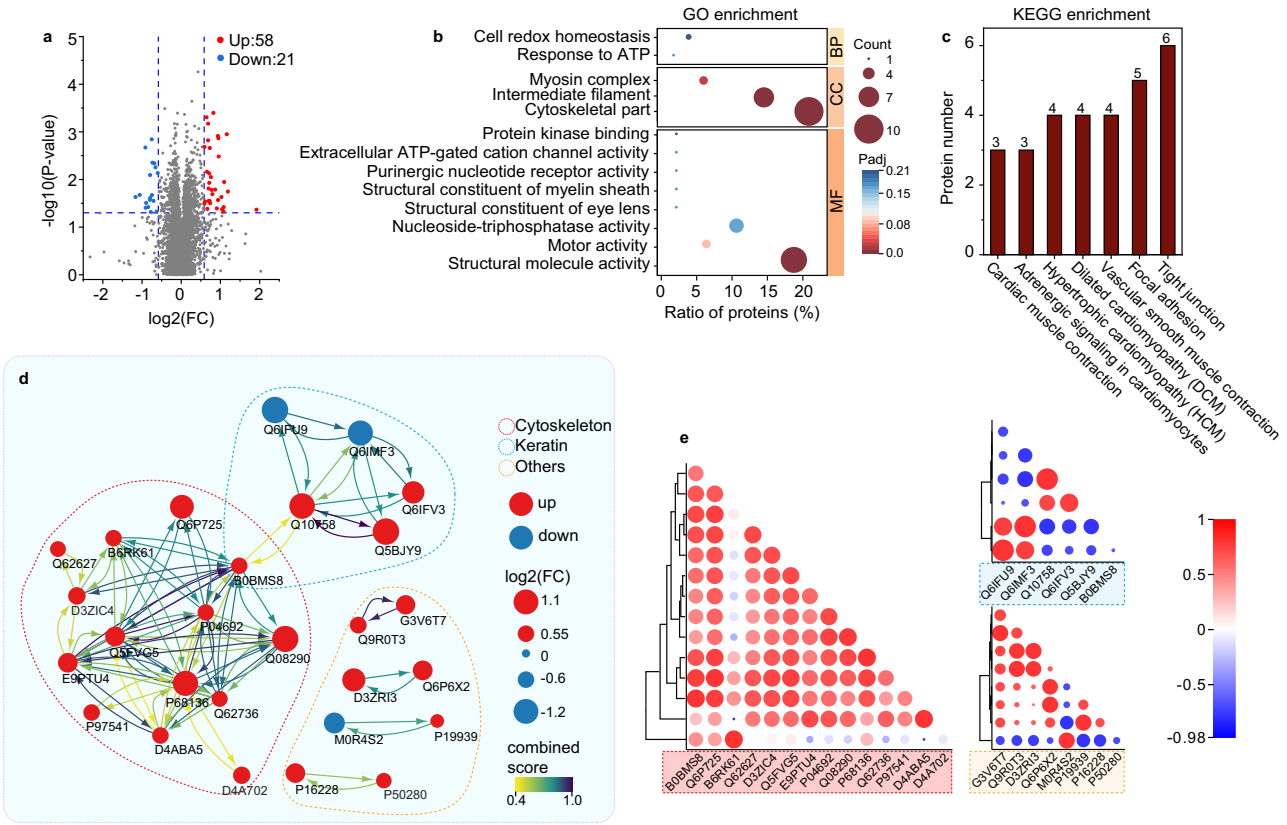

Fig. 9 | The repair reason for TB on MPG injury between the TB and injury groups. a Volcano plots of DEPs between two groups. **b**–**d** GO, KEGG enrichment, and PPI network of DEPs between two groups. The cytoskeleton proteins are circled by a red dot line, keratins are circled by a blue dot line, and others are circled by a yellow dot line. **e** The related heatmaps are based on the PPI topology network. Red dots indicate up-regulated proteins, and blue dots indicate down-regulated proteins. The dotted line color corresponds with the PPI categories. $n = 3$. A two-tailed t-test was conducted on the relative quantitative values of each protein in two comparison samples, followed by multiple comparisons with Bonferroni correction. Upregulated proteins: FC ≥ 1.5 and p value ≤ 0.05. Downregulated proteins: FC ≤ 0.67 and p value ≤ 0.05. Source data are provided in NC._data_file_s1.

effective cell loading, while the strength fibers provide a bandage-like property for ease of use. The flexibility of the TB minimizes the risk of damage to surrounding tissues. Additionally, TJs formed within the TB prevent cell leakage and protect the cells from the in vivo environment. Exosomes secreted from TB can mediate the microenvironment. High-density induced contact inhibition plays a crucial role in preventing the tumor formation of TB in vivo. RNA-seq has further revealed TB's potential to stimulate angiogenesis and promote neural repair, making it highly suitable for nerve regeneration applications. The 3D printing process for TB is time-saving, cost-effective, and allows easy structural modifications to meet diverse tissue requirements. Meanwhile, its ability to accommodate various cell types makes it a versatile cell delivery system, suitable for applications including nerve repair, oral mucosa treatment, wound healing, drug delivery, and organoid formation. TB can also be effectively stored in commercial SFCM for 5 months while retaining its repair effects, endowing TB with product conversion performance. Its biodegradable nature and lack of chemical modifications streamline FDA approval processes. However, considering the limitations of HUVECs in clinical translation, it is further to consider Mesenchymal stem cells (MSCs) as an alternative candidate for clinical translation.

The MPG crush model caused typical NB symptoms of urinary retention and incontinence[11]. The irregular distribution of more minor voiding spots indicates urinary incontinence in the scaffold and injury groups, while the TB group shows milder conditions with larger and collected spots. Urodynamic tests show that the TB group has voluntary voiding and emptying ability, although ECP has low frequencies. In contrast, the scaffold and injury groups exhibited ECP deficiency and urine leakage, indicating a loss of voluntary voiding and incontinence of overflow. Additionally, prolonged urinary retention can increase bladder compliance, resulting in adverse structural changes and potential renal failure caused by urine reflux[17]. The PCL scaffold helps deliver cells but does not directly treat MPG injury. TB therapy has effectively alleviated NB symptoms by reducing bladder issues and maintaining bladder structure. Based on MPG evaluation, crush ganglia are characterized by the loss of neurons and fibers, bleeding, inflammation, Nissl bodies reduction, axonal degeneration, and demyelination. However, wrapping TB on MPG at the junior stage can effectively deliver HUVECs with upregulated VEGFA to enhance angiogenesis for rescuing damaged nerves and preserving nerve integrity. Thereby reducing damage to functional neurons and axons. Moreover, MS protection is advantageous for facilitating the transmission of neural signals between the MPG and bladder[55]. Based on a comprehensive analysis of residual urine volume, functional and behavioral evaluation, and MPG and bladder pathology, we believe that bladder function significantly improved in TB group.

A crush injury imposes mechanical trauma to MPG, affecting their structure and essential functions such as movement, growth, protein synthesis, and homeostasis within the cell. The injury triggers immune response, which can disrupt normal lipometabolism, leading to the breakdown of lipids in Schwann cells and the myelin sheath[56]. Additionally, the injury can interfere with ion transport, impeding energy supply, fatty acid metabolism, and neural signal transmission. Ultimately, these factors contribute to cell death and dysfunction in MPG[57]. The combined impact of these challenges complicates the repairing process of MPG.

Cytoskeleton proteins play vital roles in cell fundamental functions, further facilitating repair and regeneration processes[58]. In TB group, there is an upregulation of cytoskeletal proteins that help maintain cellular structure, resist external stress, and assist in intracellular reorganization[59]. Keratins contribute to cell mechanical strength, supporting the formation of new cytoskeleton and cell connections, promoting neuron recovery[54]. Moreover, the increase in the synthesis and aggregation of contractile proteins enhances cell structural stability. This response to mechanical stimulation aids in preserving cellular equilibrium, reducing the impact of external forces, and preventing further damage in MPG. Combined with the available evidence, the effective repair of MPG results from a synergistic combination of increased angiogenic factors, efficient intercellular signaling through exosomes, and enhanced mechanical support via cytoskeletal reorganization.

While the efficacy of TB in recovering ganglia damage is notable, it requires improvement in some aspects. The immune response is one of the critical factors in ganglia injury. MSCs offer a promising alternative to HUVECs due to their immunoregulatory potential[60]. Furthermore, exosomes have emerged as a new method for delivering drugs and targeted therapy, serving as an alternative to stem cell therapy[61]. The function of the rectum and sexual organs should also be evaluated, as MPG also innervates the rectum, penis and clitoris[62–64]. Further research is needed to determine the efficacy of TB in managing central-type NB. Even though current medical interventions do not necessarily restore regular urinary function, the conduct used can be adjuvant treatments to optimize the efficiency of TB and improve the patient's life quality. Further research efforts are necessary to gain a deeper understanding of the safety and efficacy of TB for MPG impairment. In the future, a more convenient and intelligent bandage should be developed based on the TB foundation.

To the best of our knowledge, TB represents the first efficient remedial method for MPG impairment. It offers several advantages, including flexibility, operability, degradability, cryopreservability, and convertibility, making it a promising candidate for product conversion. By effectively safeguarding the MPG, TB helps prevent more severe injury early and alleviates bladder dysfunction resulting from upstream ganglia impairment. This helps preserve bladder function, structure, and voiding behavior. Our model comprehensively explains bladder and ganglia changes following MPG injury. However, further research is required to elucidate the deeper mechanism of MPG injury and validate the efficacy of these cell delivery platforms in human clinical trials. The ultimate objective is to develop a safe and effective treatment that addresses clinical needs and enhances the quality of life for patients with bladder dysfunctions caused by MPG injury. This study is of significant importance and has the potential to impact patient outcomes positively.

Methods

Bandage fabrication and evaluation

The MEW (BP6601, Yongqinquan Intelligent Equipment Co., Ltd., China) additive manufacturing system was employed to fabricate a bilayer structure using PCL (EFL-PCL-80K, Yongqinquan Intelligent Equipment Co., Ltd., China). The basal layer features mini fibers with "✳" shape node. The strength fibers are arranged in parallel lines. Pore size analysis was performed by Fiji ImageJ software and Origin 2023b.

Tensile test

A 5 mm × 20 mm rectangle border with 500 μm diameter was deposited on the non-strength and strength membranes to form a unit for tensile testing. Using a tensile testing machine (Zwick GmbH & Co. KG, Germany) to test the mechanical strength of the scaffold.

TB construction

A bandage unit was constructed using a 6 mm × 6 mm or 6 mm × 12 mm frame with a 500 μm diameter. Following disinfection in 75% alcohol for over 4 h and washing with PBS, various HUVECs (PCS-100-013, ATCC) seeding numbers (100k, 300k, and 500k) were evaluated on the 6 mm × 6 mm unit. After seeding at a high density for 1.5 h, the unit was moved to fresh medium, and the remaining cells were collected and quantified. Subsequently, cell counts were recorded after 1, 3, and 5 days to determine the optimal seeding density. Images were captured at 1.5 h, 1 day, 3 days, and 5 days to assess the confluency ratio. For more details, refer to Fig. S1 and Supplementary Movie 2.

TB proliferation evaluation

An EdU kit (Beyotime, C0071S) was applied to assess cell cycle. The samples were incubated with a medium containing 10 μM/mL EdU for 2 h, followed by fixation with 4% PFA for 15 min. After washing with 3% BSA three times, the samples were incubated with 0.3% Triton X-100 for 15 min. Subsequently, a click reaction solution was applied for 30 min, followed by another wash with 3% BSA. Dapi staining was carried out for 10 min, and the samples were observed using confocal microscopy. Cells were processed for flow cytometry analysis following the EdU incubation, with subsequent procedures as outlined in the flow cytometry section. To assess cell proliferation, the samples were treated with 500 μL of CCK8 solution (1:10, Beyotime, C0037) for 2 h in an incubator, and then readed by Microplate reader at 450 nm (Molecular Devices, America).

TB viability evaluation after long-term storage

TB was preserved long-term in either a commercial serum-free cryopreservation medium (SFCM, MeilunBio, MA0401_A) or a DMSO frozen stock solution (10% v/v DMSO) at −196 °C (liquid nitrogen). Viability assessments of the TBs were conducted at 3 weeks (DMSO-3w and SFCM-3w), 5 months (SFCM-5m), and 1 year (SFCM-1y). TBs were cultured in an incubator for 2 h to stabilize after rapid thawing. Control groups included cells on petri dishes (2D) and fresh TB (Fresh). The samples were incubated with a live/dead staining solution (1:1000, Beyotime, C2015M) for 30 min at room temperature, followed by analysis using LSM 880 (Zeiss, Germany) and CytoFlex LX (Beckman Coulter, America) to assess viability. We evaluated the effectiveness of TB cryopreservation over an 8-week period in the model.

Antibodies

Antibodies used for immunofluorescence staining, flow cytometry, and immunohistochemistry staining are reported in Supplementary Table 1.

Immunofluorescence staining

The TB and MPG sections were fixed with 4% PFA for 10 min and washed with PBS thrice. It was then blocked in 1% BSA for 40 min and stained with primary antibodies at 4 °C overnight. After washed with PBS thrice, de corresponding secondary antibodies were incubated for 1 h at room temperature. Finally, Dapi was incubated for 5 min. The images were captured by LSM 880 with a 20× objective.

Scanning electron microscope measurement

The matured TB was fixed with 2.5% glutaraldehyde at 4 °C overnight and washed with PBS 15 min trice. Osimic acid fixed for 2 h in the fume cupboard and washed with PBS for 15 min trice. Dehydrate using graded ethanol: 30%, 50%, 70%, 80%, 90%, 95%, 100%, 15 min per gradient. Dried in a vacuum oven and stored at room temperature. Following gold sprayed, the TB was imaged on the SU 8010 (Hitachi, Japan).

Transmission electron microscope measurement

The TB was fixed with 2.5% glutaraldehyde. They were prepared similarly to SEM samples, with a slight modification. After drying with graded ethanol, the samples underwent two 20 min treatments with acetone. Subsequently, they were treated with a mixture of embedding agent and acetone (V/V = 1/1) for 1 h, followed by (V/V = 3/1) for 3 h.

Finally, the samples were treated with pure embedding agent overnight. The TJs were observed using the Talos L120C TEM (Thermo Scientific, America). The MPG samples and scaffold degradation at 2w were collected and processed using the same procedure as the TB.

Flow cytometry

After 5 days of culture, cells were digested and collected from the bandage. The cell concentration was adjusted to 10^6 /mL following cell counting. Subsequently, the cell suspension was fixed with 4% PFA for 5 min and washed with PBS three times. The cells were blocked in 1% BSA in PBS for 40 min. Following this, the cells were stained with a primary antibody for 2 h at room temperature. After washing with PBS three times, the corresponding secondary antibodies were applied and incubated for 1 h at room temperature. Acquisition was performed using the CytoFlex LX, and further analysis was conducted using FlowJo.

Evaluation of TB scaffold degradation

Scaffolds were implanted on the rats' backs, collected at 2, 4, 6, and 12 weeks, then embedded in paraffin. H&E staining was conducted, and images were captured using VS200 (Olympus, Japan) at 20× objective. The samples at 2 weeks were taken for TEM preparation and testing.

Transcriptomic analysis

RNA sequencing, including RNA isolation, library preparation, and FASTQ file generation, was done by the DNA link. Total RNAs were isolated from the TB and petri dish. The visualization of gene expression, Spearman's correlation, and gene network were assessed with the FASTQ file.

Cells luciferase transfection and in vivo imaging

Transfection followed the manufacturer's instructions (Hanbio Biotechnology Co., Ltd., China). HUVECs were seeded in a 6-well plate at a density of 2.5×10^5 cells per well. After 24 h, the medium was replaced with 125 μL of Lentivirus (HBLV-LUC-ZsGreen-PURO, viral titer = 1.0×10^8 TU/mL, multiplicity of infection = 50). 24 h later, we changed the fresh medium. Forty-eight hours later, successful transfection was observed using a fluorescence microscope. Upon passaging, 5 μg/mL puromycin was added for 24 h to screen and purify cells. They were seeded in a scaffold to serve as a TB indicator.

Then, we applied it in rat models and measured at 1, 3, 5, and 8 days. Intraperitoneal injections of 15 mg/mL Luciferin (Thermo Scientific, L2916) were administered for 5 min before exposing MPG. Bioluminescence imaging was conducted using an IVIS Lumina K Series III (PerkinElmer, America), and image radiance values were analyzed using Living Image.

Animal experiments and grouping

The Institutional Animal Care and Use Committee (IACUC) of ZJCLA approved all animal experiments under protocol ZJCLA-IACUC-20010383. Male Sprague Dawley rats, aged 8–10 weeks, weighted 250–280 g, were housed with a 12-h light/dark cycle and provided free access to water and regular chow.

A total of 40 male rats were randomly divided into four groups for the experiment. The Sham group only exposed MPG, the Injury group underwent bilateral MPG crush, the Scaffold group received scaffold treatment on the damaged MPG, and the TB group was wrapped with TB. Due to the potential bladder inflammation caused by functional testing involving a bladder fistula, which may not accurately represent the actual bladder condition. Ten animals were divided into two groups of five based on whether functional testing had been conducted. Bladder samples without functional testing were selected for sampling, slicing, and subsequent analysis. Four samples were collected from each group for the MPG samples and fixed in 2.5% glutaraldehyde for TEM analysis. Six samples from each group, excluding the scaffold group, underwent TMT testing. Bilateral MPGs from the same animal were utilized as a sample set for TMT protein analysis to achieve the required protein concentration for TMT detection. Furthermore, six MPG samples were randomly excluded from the scaffold group to maintain consistency in sample size. The remaining 10 MPGs from each group were processed by first fixing them with 4% PFA and then dividing them into two groups for different treatment methods, including frozen sections and paraffin embedding.

The detailed surgical process was supplied in Supplementary Movie 2. Briefly, anesthetized with 2% pentobarbital sodium, rats were placed supine, and a midline incision was made to expose the bladder, prostate, and seminal vesicle. The dorsolateral lobe of the prostate gland usually houses the MPG, which was clamped with No. 5 Dumont forceps for 30 s after separating from the pelvis. Translucent marks were left on the surface of MPG after clamping. The TB or scaffold was separated from the unit by a punching forcep and wrapped up the injured MPG. The bladder, prostate, and seminal vesicles were restored to their original positions. The contralateral side was modeled identically to ensure accuracy and consistency among experiments. Finally, the abdominal cavity was closed with a 4-0 nonabsorbable suture. This MPG crush model simulates clinical practice and can be defined as iatrogenic NB.

Void spot assay

The void spot assay was conducted following established procedures[65]. After a 2-week treatment period, rats were individually placed in a 21×15 cm^2 cage with a rectangular board surface. They were allowed free access to food and water during a 12-h acclimation period. Urine output was measured for 6 h on filter paper, which was subsequently photographed under ultraviolet light, converted to grayscale, and analyzed using ImageJ. The area and number of individual spots and the total area of urine spots were recorded[52].

Urodynamic test

Following the assessment of changes in voiding behavior, we proceeded to evaluate urodynamic alterations. Cystostomy was performed as a preparatory step for the urodynamic test. The bladder cystostomy procedure and urodynamic testing process are visually detailed in Supplementary Movie 3.

Under isoflurane anesthesia, a subcutaneous tunnel was created from the pelvic cavity to the neck. Subsequently, laparotomy was performed to expose the bladder, and two polyethylene catheters (PE50) were implanted at the top of the bladder using purse string suture[66]. The operation's success was verified by ensuring the smoothness of the pipeline.

Following a 24 h adaptation period in rats, urodynamic testing was conducted. The rat was placed in a restricted metabolic cage, and the bladder was perfused with 0.9% NaCl solution at a constant filling rate of 6 mL/h for 30 min. Subsequently, bladder instillation commenced, and intravesical pressure and total urine weight were recorded over a 30 min period. Recording continued for an additional 5 min after bladder instillation ceased. At least three micturitions were collected during the 40 min recording period. Repeatable voiding cycles were analyzed, encompassing baseline pressure, max effective contraction peak (ECP), mean ECP, ECP variation, total voiding number, max effective urine output (EUO), mean EUO, and total EUO.

Histological staining

The MPG and bladder were collected after 2 weeks. The Zhejiang University Department of Histomorphology assisted in the embedding and sectioning of the samples. The samples underwent fixation in 4% PFA at 4 °C for 24 h, dehydration using ethanol, paraffin-embedding, and sectioning into 5 μm sections. The bladder sections were subjected to H&E and Masson staining. The MPG sections underwent H&E

and toluidine blue staining. Subsequently, the sections were overview scanned using VS200 at 20× objective. Image analysis was done via Fiji ImageJ software and Origin 2023b.

Immunohistochemistry staining

The sections were bathed in 3% H_2O_2 for 10 min and boiled for 15 min at 95 °C to recover the antigen. Following three washes with PBS, the sections were blocked with 1% BSA for 10 min and then incubated with the primary antibody at 4 °C overnight. After another round of PBS washes, the sections were incubated with the secondary antibody at 37 °C for 30 min. Subsequently, a chromogenic substrate was used to visualize the antibody-antigen complex. CD31, CD86, and CD206 were used for MPG section. CD31 and CKpan used for the bladder section. Images were captured using a VS200 with a 20× objective to scan the whole section. Image analysis was done via Fiji ImageJ software and Origin 2023b.

Proteomics

The purified peptides from MPG were analyzed using TMT on a Q Exactive HF-X Hybrid Quadrupole-Orbitrap Mass Spectrometer (Thermo Scientific), which Novogene Co., Ltd, performed. Proteins and peptides were identified using a hybrid database from the Rattus norvegicus uniport 2021.7.15.fasta (36213 sequences) database.

Statistics and reproducibility

Statistical analyses were performed using Origin 2023b software. Box and whisker plots show median and interquartile range (minima, 25th and 75th percentile, and maxima). Bar graphs show data as means ± SEM. According to the range of the upper and lower quartiles in the box diagram, data points exceeding the upper and lower limits can be considered outliers and removed. A two-tailed *t*-test was employed to compare two groups, followed by multiple comparisons with Bonferroni correction. Comparison involving more than two groups entailed one-way ANOVA, followed by a variance homogeneity test with Levene correction and multiple comparisons with Bonferroni correction. All histological assessments were performed blinded.

Representative experiments in Fig. 2o, p were repeated three times. Representative experiments in Figs. 6a–d and 7a–d, were repeated over 3 sections using VS200 Slideview or confocal microscopy in five rats.

Reporting summary

Further information on research design is available in the Nature Portfolio Reporting Summary linked to this article.

Data availability

All data supporting the findings of this study are available within the article and its Supplementary files. Any additional requests for information can be directed to the corresponding authors, who will fulfill them. Source data are provided in NC_data_file_s1. Source data are provided with this paper.

References

1. Panicker, J. N., Fowler, C. J. & Kessler, T. M. Lower urinary tract dysfunction in the neurological patient: clinical assessment and management. *Lancet Neurol.* **14**, 720–732 (2015).
2. Kaufmann, A. & Kurze, I. Diagnostik der neurogenen Blasenfunktionsstörung. *Urologe* **51**, 168–178 (2012).
3. Pelosi, G. et al. Study on the prevalence of neurogenic bladder in Brazilians with traumatic and non-traumatic spinal cord injury. *J. Spinal Cord. Med.* **46**, 677–681 (2023).
4. Gacci, M. et al. Latest evidence on post-prostatectomy urinary incontinence. *J. Clin. Med.* **12**, 1190 (2023).
5. Laterza, R. M. et al. Bladder function after radical hysterectomy for cervical cancer. *Neurourol. Urodyn.* **34**, 309–315 (2015).
6. Andersson, K.-E. & Arner, A. Urinary bladder contraction and relaxation: physiology and pathophysiology. *Physiol. Rev.* **84**, 935–986 (2004).
7. Panicker, J. N. Neurogenic bladder: epidemiology, diagnosis, and management. *Semin. Neurol.* **40**, 569–579 (2020).
8. Plotti, F. et al. Update on urodynamic bladder dysfunctions after radical hysterectomy for cervical cancer. *Crit. Rev. Oncol. Hematol.* **80**, 323–329 (2011).
9. Coolen, R., Groen, J. & Blok, B. Electrical stimulation in the treatment of bladder dysfunction: technology update. *Med. Devices* **12**, 337–345 (2019).
10. Noshadi, I. et al. In vitro and in vivo analysis of visible light crosslinkable gelatin methacryloyl (GelMA) hydrogels. *Biomater. Sci.* **5**, 2093–2105 (2017).
11. Dewulf, K. et al. Functional and molecular characterisation of the bilateral pelvic nerve crush injury rat model for neurogenic detrusor underactivity. *BJU Int.* **123**, E86–E96 (2019).
12. Hatakeyama, M., Ninomiya, I. & Kanazawa, M. Angiogenesis and neuronal remodeling after ischemic stroke. *Neural Regen. Res.* **15**, 16–19 (2019).
13. Cen, L.-P. et al. Human periodontal ligament-derived stem cells promote retinal ganglion cell survival and axon regeneration after optic nerve injury. *Stem Cells* **36**, 844–855 (2018).
14. Huang, J. et al. Endothelial cell-derived exosomes boost and maintain repair-related phenotypes of Schwann cells via miR199-5p to promote nerve regeneration. *J. Nanobiotechnology* **21**, 10 (2023).
15. Lee, Y.-C., Chang, Y.-C., Wu, C.-C. & Huang, C.-C. Hypoxia-preconditioned human umbilical vein endothelial cells protect against neurovascular damage after hypoxic ischemia in neonatal brain. *Mol. Neurobiol.* **55**, 7743–7757 (2018).
16. Grasman, J. M. & Kaplan, D. L. Human endothelial cells secrete neurotropic factors to direct axonal growth of peripheral nerves. *Sci. Rep.* **7**, 4092 (2017).
17. Bayaraa, O. et al. Nanoceria-GO-intercalated multicellular spheroids revascularize and salvage critical ischemic limbs through anti-apoptotic and pro-angiogenic functions. *Biomaterials* **292**, 121914 (2023).
18. Yorukoglu, A. C., Kiter, A. E., Akkaya, S., Satiroglu-Tufan, N. L. & Tufan, A. C. A concise review on the use of mesenchymal stem cells in cell sheet-based tissue engineering with special emphasis on bone tissue regeneration. *Stem Cells Int.* **2017**, e2374161 (2017).
19. Gao, Q. et al. 3D printed multi-scale scaffolds with ultrafine fibers for providing excellent biocompatibility. *Mater. Sci. Eng. C Mater. Biol. Appl.* **107**, 110269 (2020).
20. Kolednik, O., Predan, J., Fischer, F. D. & Fratzl, P. Bioinspired design criteria for damage-resistant materials with periodically varying microstructure. *Adv. Funct. Mater.* **21**, 3634–3641 (2011).
21. Dias, J. R., Sousa, A., Augusto, A., Bártolo, P. J. & Granja, P. L. Electrospun polycaprolactone (PCL) degradation: an in vitro and in vivo study. *Polymers* **14**, 3397 (2022).
22. Puliafito, A. et al. Collective and single cell behavior in epithelial contact inhibition. *Proc. Natl Acad. Sci. USA* **109**, 739–744 (2012).
23. Tornavaca, O. et al. ZO-1 controls endothelial adherens junctions, cell-cell tension, angiogenesis, and barrier formation. *J. Cell Biol.* **208**, 821–838 (2015).
24. Lertkiatmongkol, P., Liao, D., Mei, H., Hu, Y. & Newman, P. J. Endothelial functions of platelet/endothelial cell adhesion molecule-1 (CD31). *Curr. Opin. Hematol.* **23**, 253–259 (2016).
25. Shih, Y.-T. et al. Vinculin phosphorylation impairs vascular endothelial junctions promoting atherosclerosis. *Eur. Heart J.* **44**, 304–318 (2023).
26. Schwayer, C. et al. Mechanosensation of tight junctions depends on ZO-1 phase separation and flow. *Cell* **179**, 937–952.e18 (2019).
27. Cichon, C., Sabharwal, H., Rüter, C. & Schmidt, M. A. MicroRNAs regulate tight junction proteins and modulate epithelial/endothelial barrier functions. *Tissue Barriers* **2**, e944446 (2014).

28. Pegtel, D. M. & Gould, S. J. Exosomes. *Annu. Rev. Biochem.* **88**, 487–514 (2019).
29. Giannotta, M., Trani, M. & Dejana, E. VE-cadherin and endothelial adherens junctions: active guardians of vascular integrity. *Dev. Cell* **26**, 441–454 (2013).
30. Germain, S., Monnot, C., Muller, L. & Eichmann, A. Hypoxia-driven angiogenesis: role of tip cells and extracellular matrix scaffolding. *Curr. Opin. Hematol.* **17**, 245–251 (2010).
31. Jiang, W. et al. Enolase2 and enolase1 cooperate against neuronal injury in stroke model. *Neurosci. Lett.* **747**, 135662 (2021).
32. Saito, S. & Takeshima, H. DNER as key molecule for cerebellar maturation. *Cerebellum* **5**, 227–231 (2006).
33. Karin, M., Liu, Z. G. & Zandi, E. AP-1 function and regulation. *Curr. Opin. Cell Biol.* **9**, 240–246 (1997).
34. Miyoshi, H., Ajima, R., Luo, C. T., Yamaguchi, T. P. & Stappenbeck, T. S. Wnt5a potentiates TGF-β signaling to promote colonic crypt regeneration after tissue injury. *Science* **338**, 108–113 (2012).
35. Arenas, E. Wnt signaling in midbrain dopaminergic neuron development and regenerative medicine for Parkinson's disease. *J. Mol. Cell Biol.* **6**, 42–53 (2014).
36. Kim, E. H., Larson, J. A. & Andriole, G. L. Management of benign prostatic hyperplasia. *Annu. Rev. Med.* **67**, 137–151 (2016).
37. Rodriguez-Nieves, J. A. & Macoska, J. A. Prostatic fibrosis, lower urinary tract symptoms, and BPH. *Nat. Rev. Urol.* **10**, 546–550 (2013).
38. Dail, W. G. The pelvic plexus: innervation of pelvic and extrapelvic visceral tissues. *Microsc. Res. Tech.* **35**, 95–106 (1996).
39. Bertrand, M. M. & Keast, J. R. Dissection of pelvic autonomic ganglia and associated nerves in male and female rats. *J. Vis. Exp.* **157**, 60904 (2020).
40. Liu, B. et al. Myelin sheath structure and regeneration in peripheral nerve injury repair. *Proc. Natl Acad. Sci. USA* **116**, 22347–22352 (2019).
41. da Silva, B. R., de Melo Reis, R. A. & Ribeiro-Resende, V. T. A comparative investigation of axon-blood vessel growth interaction in the regenerating sciatic and optic nerves in adult mice. *Mol. Neurobiol.* **61**, 2215–2227 (2023).
42. Bouhrara, M. et al. Age-related estimates of aggregate g-ratio of white matter structures assessed using quantitative magnetic resonance neuroimaging. *Hum. Brain Mapp.* **42**, 2362–2373 (2021).
43. Zeng, H. & Sanes, J. R. Neuronal cell-type classification: challenges, opportunities and the path forward. *Nat. Rev. Neurosci.* **18**, 530–546 (2017).
44. Russell, F. A., King, R., Smillie, S.-J., Kodji, X. & Brain, S. D. Calcitonin gene-related peptide: physiology and pathophysiology. *Physiol. Rev.* **94**, 1099–1142 (2014).
45. Persson, K., Alm, P., Uvelius, B. & Andersson, K. E. Nitrergic and cholinergic innervation of the rat lower urinary tract after pelvic ganglionectomy. *Am. J. Physiol.* **274**, R389–R397 (1998).
46. Castro, R. et al. Specific labeling of synaptic schwann cells reveals unique cellular and molecular features. *Elife* **9**, e56935 (2020).
47. Nguyen, V. T. et al. Choline acetyltransferase, acetylcholinesterase, and nicotinic acetylcholine receptors of human gingival and esophageal epithelia. *J. Dent. Res.* **79**, 939–949 (2000).
48. Zheng, W. et al. Acetylcholine ameliorates colitis by promoting IL-10 secretion of monocytic myeloid-derived suppressor cells through the nAChR/ERK pathway. *Proc. Natl Acad. Sci. USA* **118**, e2017762118 (2021).
49. Reynolds, B. A. & Weiss, S. Generation of neurons and astrocytes from isolated cells of the adult mammalian central nervous system. *Science* **255**, 1707–1710 (1992).
50. Karakus, S., Musicki, B., La Favor, J. D. & Burnett, A. L. cAMP-dependent post-translational modification of neuronal nitric oxide synthase neuroprotects penile erection in rats. *BJU Int.* **120**, 861–872 (2017).
51. Joo, J.-Y., Schaukowitch, K., Farbiak, L., Kilaru, G. & Kim, T.-K. Stimulus-specific combinatorial functionality of neuronal c-fos enhancers. *Nat. Neurosci.* **19**, 75–83 (2016).
52. Aijaz, A. et al. Biomanufacturing for clinically advanced cell therapies. *Nat. Biomed. Eng.* **2**, 362–376 (2018).
53. Tang, P. M.-K., Nikolic-Paterson, D. J. & Lan, H.-Y. Macrophages: versatile players in renal inflammation and fibrosis. *Nat. Rev. Nephrol.* **15**, 144–158 (2019).
54. Ehrlich, F. et al. Differential evolution of the epidermal keratin cytoskeleton in terrestrial and aquatic mammals. *Mol. Biol. Evol.* **36**, 328–340 (2019).
55. Stys, P. K. The axo-myelinic synapse. *Trends Neurosci.* **34**, 393–400 (2011).
56. Vila, I. K. et al. STING orchestrates the crosstalk between polyunsaturated fatty acid metabolism and inflammatory responses. *Cell Metab.* **34**, 125–139.e8 (2022).
57. Armstrong, R. C., Mierzwa, A. J., Marion, C. M. & Sullivan, G. M. White matter involvement after TBI: clues to axon and myelin repair capacity. *Exp. Neurol.* **275**, 328–333 (2016).
58. Zhang, X., Yin, M. & Zhang, L. Keratin 6, 16 and 17—critical barrier alarmin molecules in skin wounds and psoriasis. *Cells* **8**, 807 (2019).
59. Fletcher, D. A. & Mullins, R. D. Cell mechanics and the cytoskeleton. *Nature* **463**, 485–492 (2010).
60. English, K., French, A. & Wood, K. J. Mesenchymal stromal cells: facilitators of successful transplantation? *Cell Stem Cell* **7**, 431–442 (2010).
61. Zhang, Z. G., Buller, B. & Chopp, M. Exosomes—beyond stem cells for restorative therapy in stroke and neurological injury. *Nat. Rev. Neurol.* **15**, 193–203 (2019).
62. Ramirez-Fort, M. K. et al. Prostatic irradiation-induced sexual dysfunction: a review and multidisciplinary guide to management in the radical radiotherapy era (Part I defining the organ at risk for sexual toxicities). *Rep. Pr. Oncol. Radiother.* **25**, 367–375 (2020).
63. Lam, D. & Jones, O. Changes to gastrointestinal function after surgery for colorectal cancer. *Best. Pract. Res. Clin. Gastroenterol.* **48–49**, 101705 (2020).
64. Aurore, V. et al. Anatomy of the female pelvic nerves: a macroscopic study of the hypogastric plexus and their relations and variations. *J. Anat.* **237**, 487–494 (2020).
65. Yu, W. et al. Spontaneous voiding by mice reveals strain-specific lower urinary tract function to be a quantitative genetic trait. *Am. J. Physiol. Ren. Physiol.* **306**, F1296–F1307 (2014).
66. Weyne, E. et al. Characterization of voiding function and structural bladder changes in a rat model of neurogenic underactive bladder disease. *Neurourol. Urodyn.* **37**, 1594–1604 (2018).

Acknowledgements

We thank Qiong Huang, Jingyao Chen, and Dandan Song from the Core Facilities, Zhejiang University School of Medical for their technical support. J.H. was supported by the National Science Fund for Distinguished Young Scholars [No. 52325504] and the National Natural Science Foundation of China [Nos. 52235007, T2121004] and A Project Supported by Scientific Research Fund of Zhejiang University [No. XY2021009], L.Q. and Y.W. was supported by the National Natural Science Foundation of China [No. 81971363].

Author contributions

All authors contributed to data interpretation and revised the manuscript. Jing He and Lin Qian conducted research (hands-on conduct of the experiments and data collection). Zhuang Li and Ke Yao participated in data computing and evaluation. Lin Qian, Haibin Wei, Jiaoyan He, and Xuanhan Hu conducted the animal experiment and data analysis of urodynamics. Jing He and Yanpeng Wang conducted proteomics and the corresponding quantitative analysis and data visualization. Zhuang Li

and Jiahao Weng provided TB. Jing He, Lin Qian, and Yuan Sun conceptualized this study, designed the research, interpreted the results, and prepared the Figures. Kai Liu conducted video editing. Yong He and Dahong Zhang jointly supervised this work. Jing He wrote the paper. Yong He secured funding, and coordinated and led the project.

Competing interests
The authors declare no competing interests.

Additional information
Supplementary information The online version contains supplementary material available at https://doi.org/10.1038/s41467-024-53302-5.

Correspondence and requests for materials should be addressed to Dahong Zhang or Yong He.

Peer review information *Nature Communications* thanks Suradip Das, Petra de Graaf, and the other, anonymous, reviewer(s) for their contribution to the peer review of this work. A peer review file is available.